scientific reports

OPEN

Nitrogen and phosphorus Co-doped ZnO-CdO nanocomposite with boosted photocatalytic degradation of crystal violet

Gebru Neda[1], Abi M. Taddesse[1]✉, Isabel Diaz[2], Ahmed M. Mohammed[3], Álvaro Mayoral[4] & Jemal M. Yassin[5]✉

Nitrogen (N) and phosphorus (P) co-doped ZnO-CdO nanocomposites were synthesized from bioprecursors such as rice (*O. Sativa L.*), chickpea (*Cicer arietinum L.*), soybean (*G. max (L.) Merr*) and sesame (*Sesamum indicum L.*) through self-doping into the ZnO-CdO composite. The as synthesized composites were characterized using PXRD, XPS, TGA, SEM, Cs-corrected (S) TEM, EDS, FT-IR, AAS and UV-vis spectrophotometer. Effect of biogenic doping on the band structures of the binary heterojunction was also studied using Density Functional Theory (DFT). The theoretical results showed that NP co-doping in ZnO-CdO nanocomposite improves the absorption edge to longer wavelengths in line with the experimental finding obtained from UV-vis measurement. Biogenic NP co-doped ZnO-CdO nanocomposites showed greater photocatalytic activity compared to the undoped congeners under visible light irradiations. Comparatively, photocatalytic activity of biogenic NP co-doped ZnO-CdO samples showed the order: soybean-ZC > chickpea-ZC > rice-ZC > sesame-ZC at optimal conditions under visible light irradiation. The binary ZnO-CdO nanocomposite also showed better photocatalytic activity compared to the host crystal ZnO under the same experimental conditions. Highest photocatalytic degradation efficiency of biogenic NP co-doped ZnO-CdO could be attributed to the lower rate of recombination of the photogenerated electrons and holes as well as its lower band gap energy and good reusability.

Keywords Biogenic-doping, DFT, Photodegradation, Self-doping, Thermal decomposition, ZnO-CdO

Nanotechnology enables the manipulation of matter at molecular scale (less than 100 nm), leading to the development of new materials with specific properties and high reproducibility. An important focus on the scientific community is on the synthesis of novel nanostructured materials capable of absorbing solar photonic energy and changing it into chemical or electrical energy. This is a very challenging and relevant research direction[1–3]. These nanomaterials have diverse chemical compositions, including metals, semiconductors, polymers, carbon-based materials and organic compounds or biological substances[4,5]. One application is heterogeneous photocatalysis, which uses nanomaterials for various chemical reactions and environmental remediation, such as disinfection and water detoxification, photoreduction, water splitting, organic synthesis, and removal of gaseous pollutants[6–8]. They are also used in electrical devices, optoelectronics, flat panel display, solar cells[9–11], magnetic properties[12,13], etc. However, industrial waste products whether in liquid or gaseous form, including harmful chemicals (like herbicides, pesticides, azo dyes, and pharmaceutical wastes) and gaseous wastes (carbon dioxide, carbon monoxide, methane, and nitrogen oxides), pose serious environmental challenges and can negatively impact human health and ecosystems[14–16]. Many of these chemicals are suspected endocrine disruptors found in rivers and lakes[17,18].

Kumar et al.,[19] reported that textile dye effluents and other industrial dyes represent one of the largest groups of organic compounds that pose a growing environmental hazard, with 1–20% of the global dye production lost

[1]Department of Chemistry, Haramaya University, P.O.Box 138, Dire Dawa, Ethiopia. [2]Instituto de Catálisis y Petroleoquímica, CSIC, c/Marie Curie 2, Madrid 28049, Spain. [3]Department of Chemistry, Addis Ababa University, P.O.Box. 1176, Addis Ababa, Ethiopia. [4]Instituto de Nanociencia y Materiales de Aragón (INMA), CSIC-Universidad de Zaragoza, Calle de Pedro Cerbuna, Zaragoza 12, 50009, Spain. [5]Department of Chemistry, Debre Berhan University, P.O.Box. 445, Debre Berhan, Ethiopia. ✉email: abi.taddesse@haramaya.edu.et; abi92003@yahoo.com; jemalchemistry@gmail.com; jemalmohammed@dbu.edu.et

and/ or discharged during the dyeing process. The discharge of those colored wastewaters in the environment contributes to pollution and eutrophication, creating hazardous byproducts through chemical processes. It is important to recognize that dyes can have harmful impacts and can decrease light penetration in wastewaters[19–21]. Decolorization of these dyes has gained interest, and certain remediation methods have been preferred for this purpose. Conventional methods such as adsorption on activated carbon, reverse osmosis, coagulation using chemical agents, ultrafiltration, and ion exchange on synthetic adsorbent resins, etc. have been employed for the removal of dye contaminants[22–24]. These techniques merely succeed in moving organic effluents from the water to another phase, which then generates secondary pollution. This will need additional treatment of solid waste and regeneration of the adsorbent which will increase the overall cost of operation. Recent research has focused on using photocatalysis as an effective method for degradation of dyes found in wastewaters. This approach has shown promise in completely decomposing and mineralizing the target pollutants.

In recent years, research activities have focused on advanced oxidation processes (AOPs) as a means to destroy synthetic organic compounds that are resistant to traditional methods. AOPs generate highly reactive radicals, primarily hydroxyl radicals ($^{\bullet}HO$), utilizing various energy sources like solar and chemical energy[24,25]. Heterogeneous catalysis plays a key role in photocatalytic oxidation (PCO), enabling the partial or complete decomposition of gaseous or liquid-phase pollutants into benign byproducts,[26,27] with metal-oxide nanoparticles like TiO_2, Al_2O_3, ZnO, CdO, and MgO due to their effectiveness, low dimension and price[27–29]. TiO_2 is the one that is most frequently used for its stability, non-toxicity, and cost-effectiveness[15,30], while ZnO has also gained attention for its multi-functional advantages, including a wide direct band gap energy of 3.37 eV, which allows it to efficiently absorb and emit UV light, and a high exciton binding energy of 60 meV at room temperature, making it suitable for photocatalysts, and other applications. ZnO is considered a highly valuable industrial material due to its effectiveness as a harmless catalyst, inexpensive production costs, and environmental benignity[31–34]. It can function as a sensitizer for light-driven redox reactions due to its electronic structure, characterized by a fully occupied valence band (VB) and an empty conduction band (CB); when a photon with sufficient energy excites an electron from the valence band to the conduction band, it leaves behind a hole. The excited electrons and holes can recombine, release energy as heat, be trapped in metastable states, or react with adsorbed electron donors and acceptors, and if a suitable trapping agent or surface defect is present, recombination can be prevented, facilitating redox reactions[35,36]. However, ZnO can only absorb a small fraction of the solar spectrum in the UV region, which limits its ability to utilize visible light effectively. In contrast, CdO, with a narrower band gap (Eg = 2.2–2.7 eV), can absorb visible light but exhibits low photodegradation efficiency due to the rapid recombination of charge carriers[37,38]. Therefore, it is of significant attention to enhance the photocatalytic activity of materials under visible light[39–41].

For this reason, various investigations have been attempted to prolong the absorption range of materials into visible light region, including depositing noble metal particles, doping with transition metal ions, coupled semiconductor systems[33,42–45], and nonmetal doping and co-doping[46,47]. In order to influence the band gap, ZnO has been alloyed with various oxides such as, BeO and MgO forming $Zn_{1-x}Y_xO$, where Y can be Cd, Mg, or Be. Whereas alloying with Cd reduces the band gap energy (Eg), the other two compounds lead to an increase of Eg[48]. Doped materials are significant for band gap engineering and P-N junctions. CdO exhibited good performance attributable to its narrow direct band gap, allowing modifications in ZnO luminescence from UV to blue and green light spectra. As a result, CdO-ZnO composite reveal good photocatalytic activity under visible light[31]. Both CdO and ZnO materials have high transparency in the visible and near infrared regions of the electromagnetic spectrum and show n-type conductivity[49,50]. Doping ZnO and CdO with appropriate donors could enhance their electrical properties. ZnO thin films maintain stable electrical and optical properties; while CdO films have a lower band gap and a poor optical transmittance in the visible spectra region compared to ZnO films[51,52].

There are some reports on P and N doping on ZnO nanoparticles. But, there is no report on co-doping on CdO-ZnO nanocomposite. In this work, the biogenic NP-co-doped CdO-ZnO nanocomposite was synthesized systematically by thermal decomposition method and the prepared samples were characterized by various physical and chemical techniques. In addition theoretical study on the optoelectronic properties of these composites was studied using DFT study. The photocatalytic performance of the as-synthesized materials was also investigated using crystal violet as model organic pollutant.

Experimental section

Preparation procedures of photocatalysts

Chemicals and reagents and the preparations of both ZnO and CdO nanoparticles are described well in the Supporting Information.

Synthesis of ZnO-CdO nanocomposite

The ZnO-CdO nanocomposites with four different weight ratios of (Zn/Cd precursors = 95:5, 90:10, 85:15 and 80:20) were systematically synthesized following the method reported elsewhere[53]. In a typical synthesis, 34.71 g of zinc nitrate hexahydrate and 1.20 g cadmium nitrate tetrahydrate were mixed and ground for 1 h then annealed at 400 ºC for 3 h in a muffle furnace and denoted as ZC (95:5). Similar procedure was taken to manipulate the metal precursor proportions listed in Table S1 to synthesize the ZC (90:10), ZC (85:15) and ZC (80:20) nanocomposites. The resultant sample was denoted as ZC. For comparison purpose, physical mixture of ZnO and CdO was mixed in 90:10 weight ratios and represented as PhMx.

Synthesis of NP-co-doped ZnO-CdO nanocomposite

Four kinds of crop seeds, namely rice (*O. Sativa L.*), chickpea (*Cicer arietinum L.*), soybean (*Glycine max (L.) Merr*) and sesame (*Sesamum indicum L.*) were collected from the local market in Haramaya and employed as bio-precursors to synthesize biogenic nitrogen (N) and phosphorus (P)-co-doped ZnO-CdO nanocomposite. 15.0 g of each crop seed was taken and rinsed with pure water several times to remove the cover (coat). The coatless crop seeds were treated with 100 mL of 5% HCl solution for 12 h to get rid of K, Ca and S ions. Sesame is an exception in this treatment as removing the coat was quite difficult. So the acid treatment was done in the presence of the seed cover. The solutions were rinsed with distilled water. Then 10.0 g of as synthesized ZnO-CdO nanocomposite was taken and mixed with each of crop seeds (chickpea, rice, sesame, and soybean), respectively. The reaction was assumed to undergo grinding together by using mortar and pestle. Then the samples were dried in an oven at 80 ºC for 24 h. At this time, pure biogenic NP-co-doped ZnO-CdO is not anticipated since there is hydroxyl part in plant seeds which cannot easily be disappeared. Hence, the samples were annealed to 300 ºC for 1 h to get respective nanocomposite. The N and P in the crop seeds are assumed to self-dope into ZnO-CdO nanocomposite (Table S1) up on annealing and designated as rice-ZC, sesame-ZC, chickpea-ZC and soybean-ZC, respectively.

Characterization of As-synthesized photocatalysts

The as synthesized samples were characterized by various physicochemical techniques. Powder X-ray diffraction (PXRD) patterns were recorded in 2θ range of 4–90º using a Philips X'PERT diffractometer equipped with an X'Celerator detector and using Cu Kα radiation (λ = 1.5418Å). X-ray Photoelectron Spectroscopy (XPS) data were obtained with a SPECS GmbH system equipped with a hemispherical energy analyzer PHOIBOS 150 MCD, using a non-monochromatic Mg X-ray source (1253.6 eV) with a power of 200 W and voltage of 12 kV, with the sample being at vacuum below 5×10^{-9} mbar. Data treatment was performed with the CasaXPS program. Thermogravimetric analysis (TGA) was registered in a Perkin-Elmer TGA7 instrument, in the temperature range from 30 ºC to 900 ºC under air flow at a heating rate of 20 ºC min^{-1}. Scanning electron microscopy hyphenated with energy dispersive X-ray spectroscopy (SEM) was carried out using an ultrahigh resolution FEI-NOVA NanoSEM 230 FE-SEM instrument. Transmission electron microscopy (TEM-EDS) images were obtained in a JEOL 2000FX microscope operated with an accelerating voltage of 200 kV and a Titan ThermoFisher microscope X-Field Emission Gun (FEG), operated at 300 kV with a CEOS spherical aberration (Cs) corrector for the electron probe. Aberrations were minimized prior every experiment using a gold standard sample assuring a point-to-point resolution of 0.8 Å. The microscope was also equipped with a monochromator (not excited for the current experiments), an Oxford EDS detector and a Gatan Tridiem Energy Filter for chemical analyses. Fourier transform infrared (FTIR) spectra were recorded in a PerkinElmer FTIR spectrometer. UV-vis spectroscopy (SANYO, SP65, GALANAKAMP, U.K) measurements were run in a single beam UV-vis spectrophotometer. Atomic absorption spectroscopy (AAS, BUCK) instrument Model-210VGP, method air/acetylene, current 1.5 mA and slit 0.7 nm were determine the amount of zinc and cadmium.

Photocatalytic degradation study

To evaluate the photocatalytic activities of the samples, degradation experiments of crystal violet (CV, model pollutant) in aqueous solution was carried out in the presence of as-synthesized nanoparticles as follows: The experiments were carried out under visible light lamp using as-synthesized photocatalysts. The photocatalytic reactor consists of a glass tube with an inlet tube for provision of air purging during photocatalysis and outlet tube for the collection of samples from the reactor at regular time intervals. 1.5 g of the as-synthesized photocatalyst powder and 100 mL of aqueous solution of CV (10 mg L^{-1}) was taken in the reactor tube and the suspension was stirred in dark for 30 min to obtain adsorption/desorption equilibrium before irradiating the dye in the reactor[54]. The visible tungsten lamp (TORCH) that emit in wavelength range of 368–540 nm with the definite power 40 W, 220 V, 0.18 A and 50 Hz frequency was employed as light source and positioned parallel to reactor. The distance between the top of reactor and visible lamp was 10 cm. 5 mL of the sample was withdrawn at 20 min interval. The suspension was centrifuged at 3000 rpm for 15 min and filtered to remove the catalyst particles before measuring absorbance. The absorbance of CV solution was determined at wavelength of 590 nm. Percentage degradation of CV was calculated using the relation:[55]

$$\%\,\text{Degradation} = \frac{A_0 - A_t}{A_0}\text{x}\,100 \tag{1}$$

Where A_0 is absorbance of dye at initial stage, A_t is absorbance of dye at time 't'.

Computational study

Total energy and band structure of ZnO, $Zn_{0.9}Cd_{0.1}O$ and NP-co-doped $Zn_{0.9}Cd_{0.1}O$ nanostructures were performed by using the density functional theory (DFT) implemented in the TRANSIESTA based Atomistic Toolkit (ATK) software. In order to carryout calculations of structural and electronic properties of the samples, we have used GGA-PBE and LDA-PW approximation methods with electron density mesh cut-off 150 Rydberg and electron temperature of 300 K with double zeta polarized basis set, and the Brillouin zone integration parameters 5 × 5 × 5 k-point mesh. The full structure optimization of cell parameters and internal coordinates is performed in all super cells prior to calculations of electronic and structural parameters. Bulk NP-co-doped $Zn_{0.9}Cd_{0.1}O$ alloy studied in this work is modeled by repeating 3 × 3 × 1 hexagonal wurtzite super cell conformation with 36 atoms per super cell since $4\times3^2 = 36$, 4 atoms per unit cell.

Results and discussion

PXRD analysis of As-synthesized samples

X-ray diffraction patterns of the synthesized CdO, ZnO, PhMx (physical mixture of ZnO and CdO (90:10)), ZC (ZnO-CdO (90:10)), rice-ZC, sesame-ZC, chickpea-ZC and soybean-ZC are shown in bottom-up order in Fig. 1. The result showed the change of cadmium nitrate tetrahydrate and zinc nitrate hexahydrate to CdO and ZnO nanoparticles successfully via thermal decomposition method and the XRD pattern corresponds to cubic and hexagonal wurtzite structures (JCPDS No. 79–0208),[53] respectively. Two phases are identified in ZC (90:10 weight ratio was chosen for biogenic NP co-doped) nanocomposite sample as shown in Fig. 1. One is the hexagonal structure of ZnO with strong and narrow diffraction peaks at angles (2θ) of 31.77°, 34.41°, 36.32°, 47.61°, 56.55° and 62.82° which correspond to (100), (002), (101), (102), (110) and (103) crystal planes respectively and other is CdO with weaker diffraction peaks at angles (2θ) of 33.16°, 38.44°, and 55.43° which correspond to (111), (200) and (220) crystal planes respectively (JCPDS No. 73-2245)[53]. The rest of patterns also show that all biogenic nanocomposites (rice-ZC, sesame-ZC, chickpea-ZC and soybean-ZC) and PhMx samples possess identical XRD patterns as ZC composite sample.

In Fig. 1, the XRD diffractograms of ZC and PhMx samples, the separate diffraction peaks of both CdO and ZnO appear. Compared to pure ZnO diffraction peaks of ZC sample diffraction peaks are shifted to larger diffraction angle by 0.10°. Chickpea-ZC, rice-ZC, sesame-ZC and soybean-ZC samples diffraction peaks show shift to lower diffraction angle by 0.08°, 0.17°, 0.19°, and 0.07°, respectively compared to pure ZnO sample. This shift suggests that the oxygen or Zn atoms in the lattice of NP-co-doped ZnO samples may be substituted by other atoms. It is considered that the position of diffraction peaks in co-doped samples shift to lower diffraction angle, which may be contributed to fact that either atomic radius of N is greater than O and smaller than Zn, it is suggested that N is substituted on O sites,[56,57] and ionic radii of P^{3-} ion is larger than O^{2-} ion suggesting that substitution of O^{2-} by P^{3-};[58] or synergetic effect of both reasons. The intensity of CdO diffraction peaks (Fig. 1) are smaller than ZnO peaks in all CdO incorporated ZnO samples; particularly in PhMx, chickpea-ZC and sesame-ZC samples, it implies lower ratio of CdO in the composite; compared to four biogenic NP-co-doped samples, sesame-ZC samples diffraction peaks are smaller and broader (Table S2, $\beta_{\text{sesame-ZC}} = 0.00609^\circ$) than the rest three composites. The calculated average crystallite size (D) of the photocatalysts is given in Table S2. It is noted that all the catalysts are crystalline in nature with average crystallite sizes ranging from 25.0 to 41.6 nm (Table S2). Crystallite size of rice-ZC, PhMx, and ZC samples (Fig. 1) are larger than pure ZnO compared to chickpea-ZC, sesame-ZC and soybean-ZC samples, which are in good agreement with pure ZnO. Seeds of *O. Sativa L.* mainly contain starches (a mixture of amylases and amylopectines). Seeds of *Cicer arietinum*, *G. max (L.) Merr* and *S. indicum Linn* mainly contains proteins and fats, respectively[59].

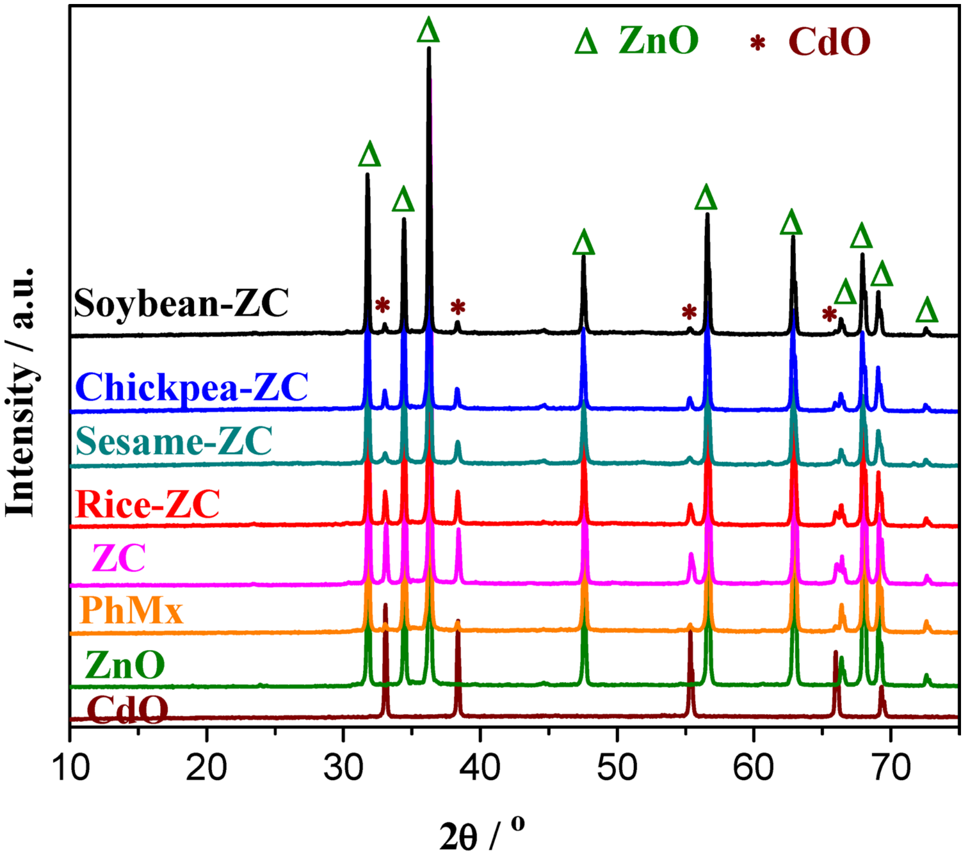

Fig. 1. X-ray diffraction patterns of the as-synthesized photocatalysts CdO (wine line), ZnO (olive), PhMx (orange), ZC (magenta), rice-ZC (red), sesame-ZC (dark cyan), chickpea-ZC (blue) and soybean-ZC (black) samples.

XPS analysis

The surface composition and chemical states of sesame-ZC composite can be determined by means of XPS spectrum according to the characteristic binding energies of the different elements on material surfaces. The XPS survey spectrum evidenced the presence of Cd, Zn, N, P, C and O core level regions as shown in Fig. 2a. From the survey spectrum Zn3d, Zn3p, Zn2p, Cd3d, Cd3p, P2p, N1s, C1s and O1s levels were observed. The material displays (Fig. 2b) a doublet at about 1024.1 and 1047.2 eV, corresponding to the Zn 2p3/2 and 2p1/2 core levels. The first peak at 1024.1 eV is attributed to Zn^{2+} ions in the oxygen deficient ZnO environment. Moreover, the Zn 2p3/2 XPS peaks are sharp[60,61]. Thus, it can be confirmed, that Zn element exist mainly in the form of Zn^{2+} on the samples surfaces.

The binding energies for the two spin-orbit components that make up the Cd 3d features-3d5/2 and 3d3/2 were found to be 407.5 and 414.2 eV (Fig. 2c), respectively. The binding energy of Cd 3d5/2 is ascribed to the Cd^{2+} bonding state in a good agreement with the earlier report. Fig. 2d shows the O1s with two symmetric peaks at 523.5 eV and 533.5 eV. This indicates the presence of oxygen atoms integrated with both Zn and Cd on the surface, providing insights into the oxygen vacancies in the photocatalyst. These vacancies introduce defect states within the bandgap, acting as charge carriers and substantially impacting the material's electrical and optical properties. Additionally, they improve conductivity and promoting charge transfer mechanisms[61,62].

XPS characterization evidenced the presence of doped N and P in ZC composite (Fig. 2e-f). Regarding P doping, the XPS spectra of P2p show only one peak at 133.7 eV (Fig. 2e) and no peaks around 128.6 eV, indicating that P ions only exist as cations in a pentavalent oxidation state (P^{5+}), not as anions in tetravalent oxidation state (P^{3-})[60,63,64]. Regarding N1s exhibits two peaks in Fig. 2f, at 340.8 eV and 353.2 eV. Due to the N anion in the composite, in which the oxygen sites in O-Zn-O-Cd bonds are partially substituted by N atoms[65]. The second peak at 353.2 eV was attributed to molecularly chemisorbed nitrogen species. Therefore, the XPS

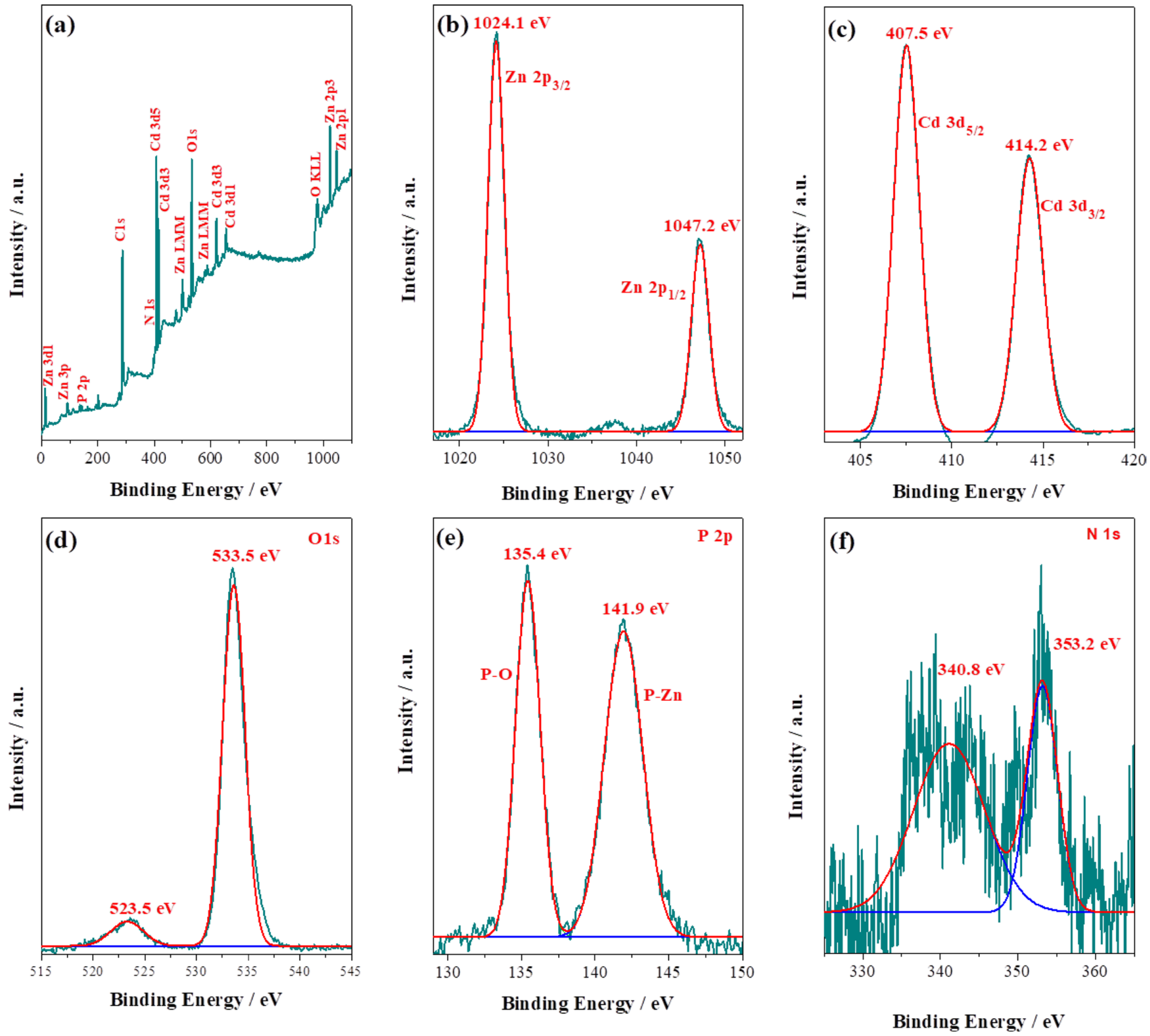

Fig. 2. XPS spectra of sesame-ZC composite (**a**) survey spectrum, (**b**) Zn 2p (**c**) Cd 3d, (**d**) O 1s, (**e**) P 2p, and (**f**) N 1s. In each graph, the simulated background (blue line), the peak components and their energy positions (red), and the enveloping line (green) arisen from the deconvolution of as-registered spectrum (dark cyan) are also given.

spectrum evidenced the XRD results of the composite materials. The TGA curve and weight loss in different regions of the as-obtained photocatalysts are shown in Fig. S1 and Table S3, respectively.

Morphology analysis

Figs. 3 and S2 shows the surface morphology of the as synthesized (CdO, ZnO, PhMx, ZC, rice-ZC, sesame-ZC, chickpea-ZC and soybean-ZC) samples as investigated by SEM. Interestingly, the SEM images of CdO exhibited a well-defined hexagonal structure. In the case of ZnO, a square pyramid structure is observed aggregated in a remarkably distinct fashion to form beautiful micro-roses (Figs. 3a-b and S2a-b). Fig. 3c shows the SEM micrograph for the physical mixture of CdO-ZnO. As can be discerned from the micrograph, the structure exhibited for both phases in the separate incidence is mimicked with no influence on one another revealing the limited interaction between the two interacting particles as the result of physical blending (Fig. 3c). In sharp contrast to this, the chemical mixture between ZnO and CdO revealed the deposition of CdO on the surface of ZnO (Figs. 3d and S2c). Upon doping, the square pyramid frame of ZnO was filled by hexagonal CdO nanoparticles. The addition of bio-precursors appeared to enhance the well dispersed deposition of CdO nanoparticles perhaps as the result of capping agents obtained from the biological dopants (Figs. 3e-h and S2d-h). The surface of the composite seems to be composed of expanded porous agglomerated structures with homogeneously distributed small sized hexagonal CdO nanoparticle due to the effects of biogenic N and P and expansion of CdO, which brings a change in the morphology of ZnO and ZC composite[66]. It is evidently observed that the size of the hexagonal like structure decreases in the NP co-doped composite due to heterogeneous nucleation effect induced by the incorporation of biogenic N and P dopants and these dopants

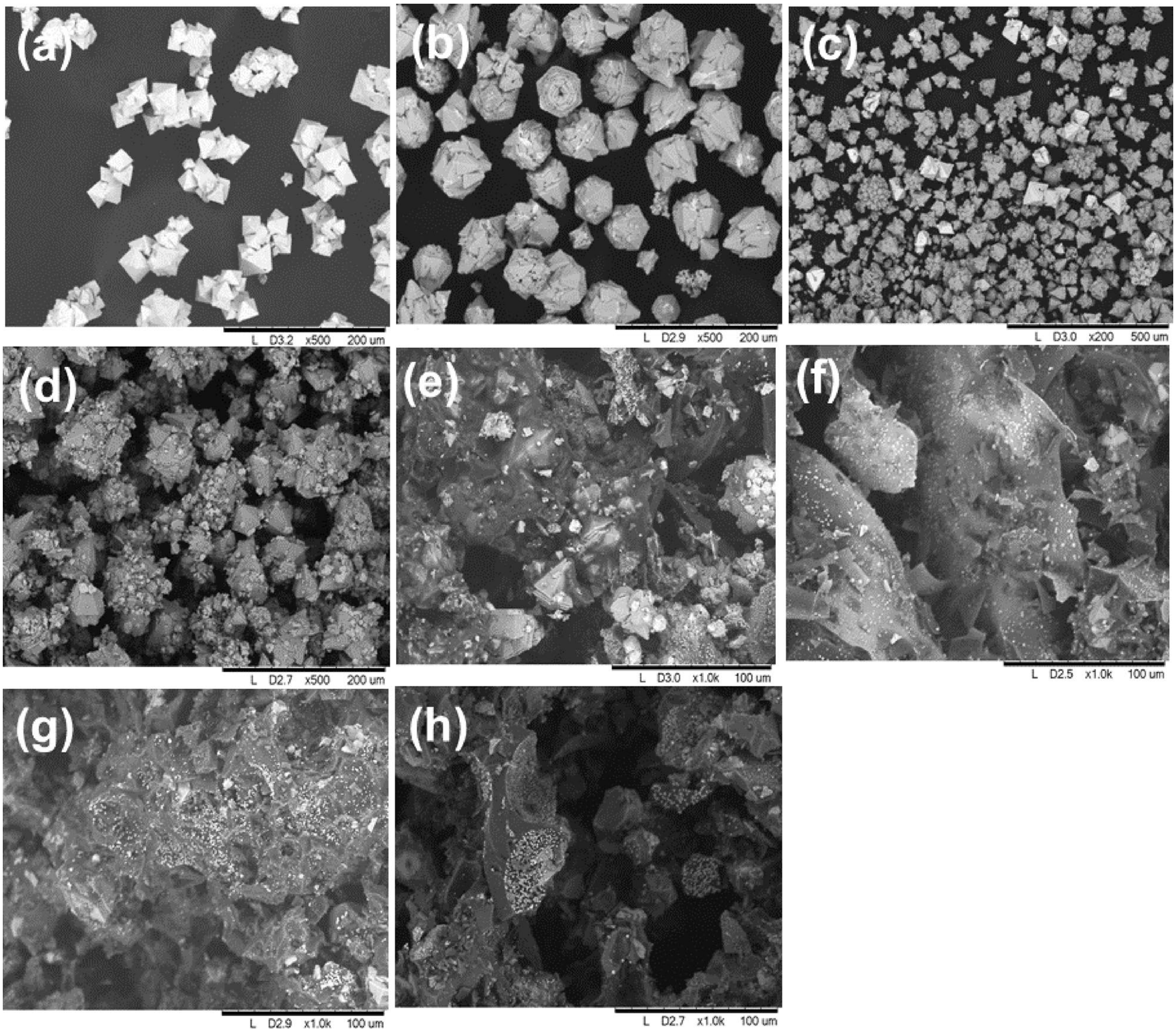

Fig. 3. SEM micrographs of (**a**) CdO, (**b**) ZnO, (**c**) PhMx, (**d**) ZC, (**e**) rice-ZC, (**f**) sesame-ZC, (**g**) chickpea-ZC and (**h**) soybean-ZC samples.

create additional nucleation sites on the surface and within the composite, promoting the formation of smaller crystalline domains[67].

To apprehend the influence of the biogenic precursor, we selected the sesame-ZC composite as representative materials to study under the advance electron microscope. The Cs-corrected Scanning TEM-HAADF (high angle annular dark field) micrograph of as obtained NP co-doped ZC nanocomposite shows the well order, uniformly sized particles and formation of well-defined morphologies (Figs. 4 and S3). It can be seen from Figs. 4a-e and S3a-f that there are some individual nanoparticles which have cylindrical and hexagonal shapes, in accordance with SEM images. It has been seen that the NP co-doped ZC nanocomposite is smooth on the surface, mostly having the diameter around in the range of 10–15 nm. The HR-STEM measurements indicated lattice fringes of 0.34 and 0.30 nm for ZnO and CdO in the sesame-ZC composite sample, confirming the presence of highly crystalline nanostructures. The inset Fast Fourier Transform (FFT) pattern (Fig. 4e) displays diffraction spots from the CdO, superimposed on bright fringes or area corresponding to ZnO, which aligns well with the XRD results. From elemental analysis (Figs. 4g and S3g) it is found that composition of nitrogen and phosphorous is 3.52% and 2.21% for rice-ZC, 2.72% and 3.87% for sesame-ZC, 7.26% and 3.29% for chickpea-ZC and 8.47% and 4.91% for soybean-ZC, respectively, which is supported the XPS results. Ions such Mg and S are evidenced here possibly due to the presence of the sesame seed cover that is resistant to the acid (5% HCl Solution) treatment

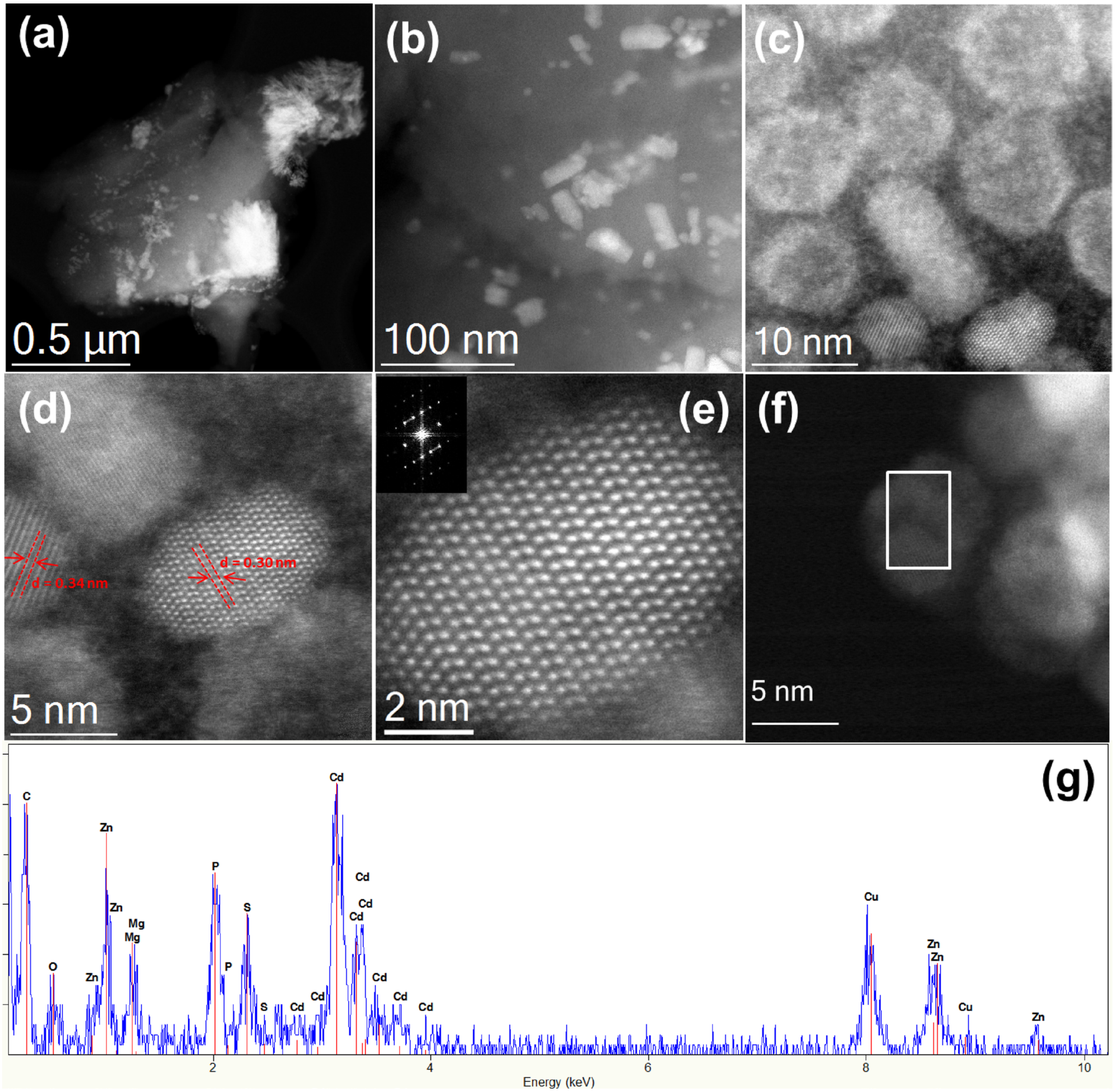

Fig. 4. Cs-corrected STEM-HAADF images (inset Fast Fourier Transform, FFT) of (**a**-**f**) sesame-ZC composite sample under different magnifications and (**g**) their EDS spectra.

used in removing ions such as K, Ca and S. The source for Cl could be the acid used for the seed treatment. Our result differs from previous reports when it comes to sulfur as the presence of this element is confirmed after acid treatment. We have also confirmed that Mg ion cannot be completely removed based on the acid treatment protocol reported[63], calling for further modification of such treatment to achieve the desired result.

FT-IR analysis

The characteristic functional groups of the photocatalysts were investigated using FT-IR spectroscopy. Fig. S4 showed the FT-IR spectra of as-synthesized photocatalysts in 4000 to 400 cm^{-1} region. For all samples, the broad absorption band around 3408 cm^{-1} corresponds to the O-H stretching vibrations of water present in ZnO; the band appears with strong intensity and shifted to the right for ZC samples, and for co-doped samples, the band slightly shifts to the right except soybean-ZC samples which shows strong shift. The other transmittance bands for all samples around 2924 cm^{-1} and 2854 cm^{-1} are assigned to a residual organic component. The band ~1627 cm^{-1} which can be associated with the bending vibrations of H_2O molecules is strongly diminished for all co-doped samples. The absorption bands between 1553 cm^{-1} and 1567 cm^{-1} in all co-doped samples are due to the carbonyl groups of the carboxylate ions which might remain adsorbed on the surface of ZnO and CdO[53]. The other bands that appear ~1166 cm^{-1} for ZC sample only with diminished intensity, ~1259 cm^{-1} for ZC, PhMx and co-doped samples with diminished intensity for later samples; and ~1384 cm^{-1} in all photocatalysts may be due to O-C-O stretching vibrations of the monodentate carbonates species originated from CO_2 [68]. The shoulders between 442 cm^{-1} and 707 cm^{-1} corresponds to distinct stretching mode of crystal ZnO[69]. Generally, Fig. S4 shows the NP-co-doped ZC spectra which are almost the same as that of the undoped ZnO nanoparticles.

UV-vis absorption measurements

The electron negativity of O (3.5) is larger than that of N (3.0), so the Zn-O band has larger ionicity than the Zn-N band. Thus, the decrease in E_g can also probably ascribe to the decrease in ionicity due to the formation of Zn-N bonds within the NP-co-doped ZC nanocomposites[70]. Atomic N and P can be incorporated as shallow acceptors, while a larger amount of native defects such as Zn interstitials (Zn_i) and oxygen vacancies (V_O) can be formed in the nanostructures which results a decrease in absorption band edge[71,72]. Concurrently, in Fig. S5, it can also be seen that that absorption edge of NP-co-doped ZC nanocomposites differs as the nitrogen content varies. The absorption edge decreases with increasing the N doping. Since the visible photocatalytic activity depends on the concentration of doped nitrogen, the absorption edge is more shifted to longer wavelength at higher doping concentration of nitrogen[73,74]. The DFT calculations also support the decrease in the absorption edge decrease due to N and P incorporation in ZC nanostructures. This dopant creates impurity levels near the conduction and valence bands, effectively narrowing the bandgap. Hence soybean-ZC sample has largest absorption onset. As it can be seen from Table S4 band gap of the synthesized NP-co-doped ZC samples are in the following order: soybean-ZC (2.16 eV) < chickpea-ZC (2.2 eV) < rice-ZC (2.28 eV) < sesame-ZC (2.32 eV). This may be due to the cumulative synergetic effect of N and P in NP-co-doped ZC. Thus, the NP-co-doped ZC can be used as an efficient photocatalyst under visible light irradiation.

The spectrum of pure ZnO and CdO are also included for comparison. ZnO and CdO sample shows the band gap absorption onset at 376 nm and 539 nm respectively, corresponding to an intrinsic absorption of ZnO and CdO, and it is in good agreement with the result reported elsewhere[53]. Absorption peak of ZnO is red shifted, as compared to the bulk exciton, which is due to the size effect of the nanostructures[75]. From Fig. S5, it is clear that absorption edges of ZC nanocomposite and PhMx samples show obvious red-shift as compared to that of pure ZnO. The red-shift was caused by the decrease of optical band gap of ZnO. It is also found that the band gap of all biogenic NP-co-doped ZC samples (Table S4) are further extended to longer wavelength as a result of N and P incorporation in ZC nanostructure, it can be associated with the formed impurity states in the band gap by the partial substitution of O with other atoms in the crystal lattice of ZC. UV-visible absorption spectra of CV dye is shown in Fig. S6. Table S5 shows the Zn and Cd metal content in the ZC nanocomposite as obtained from atomic absorption spectroscopy (AAS) analysis and corresponding calibration curves are displayed in Fig. S7a-b.

Photocatalytic studies of photocatalysts

The photocatalytic degradation of organic dyes by semiconductor catalyst under visible light irradiation typically includes two mechanisms. First one is based on the excitation of the semiconductor, which comprises excitation of the semiconductor by light irradiation to form photogenerated electron/hole pairs (electrons in the conduction band and holes in the valence band). The chemical reactions with the organic pollutants takes place as photogenerated charges move to the particle surface. The other one is based on the excitation of dye, in which the dye acts as a sensitizer of visible light and excited electrons will be transferred from the dye to an electron acceptor to become a cationic dye radical followed by self-degradation or degradation by the reactive oxidation species. In the present case, valence electrons of ZnO can be excited to the conduction band leaving behind a hole in the valance band by absorbing visible light due to the sufficiently narrow band gap of NP-co-doped ZC nanocomposite. The generated electrons react with dissolved oxygen molecules and produce oxygen peroxide radicals. The positive charge hole can react with the hydroxide ion derived from water to form hydroxyl radicals and hydrogen peroxide, and finally degrade organic pollutants into carbon dioxide and water[76].

Comparison of photocatalysts

The photocatalytic activity of ZnO, PhMx, ZC, rice-ZC, sesame-ZC, chickpea-ZC and soybean-ZC photocatalysts were evaluated by photocatalytic degradation of crystal violet (CV) dye under visible light and in dark systems. The adsorption and degradation profile of the dye, photo-catalyzed by as-synthesized samples is shown in Fig. S8 and Fig. 5, respectively.

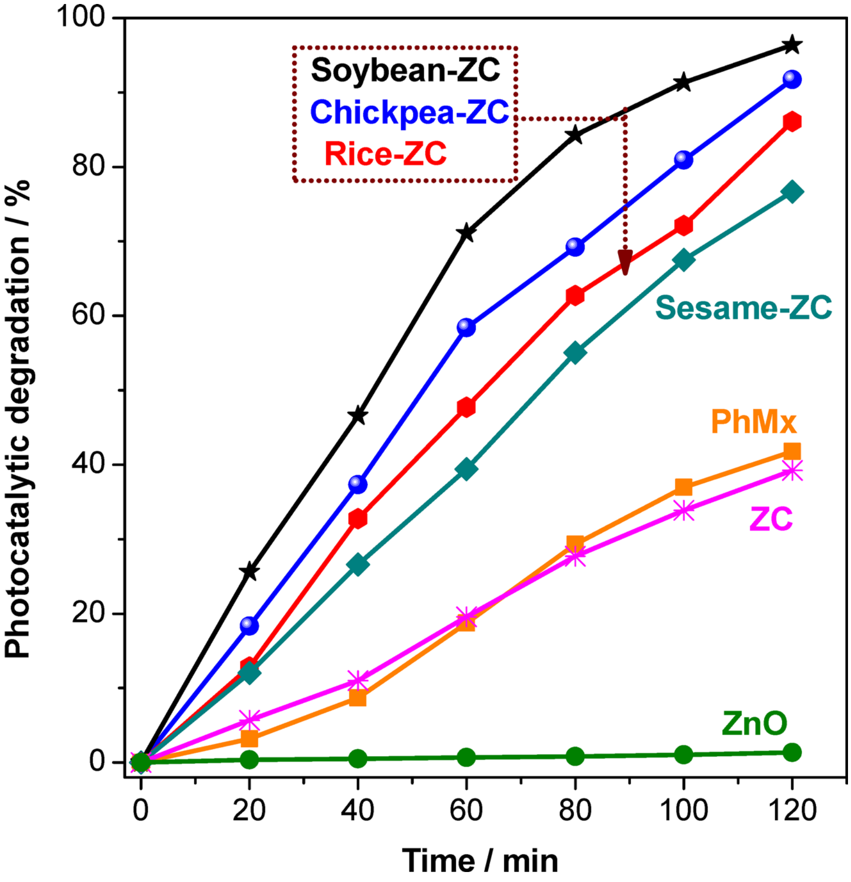

Fig. 5. Plot of percentage degradation of CV as function of time under visible irradiation using synthesized photocatalysts. Reaction conditions: initial CV concentration = 10 mg L^{-1}, catalyst load = 150 mg L^{-1}, pH = 7 and irradiation time = 120 min.

According to the results of adsorption efficiency of photocatalysts has the order: ZC < PhMx < rice-ZC < ZnO < chickpea-ZC < sesame-ZC < soybean-ZC with corresponding values, 4.57, 4.62, 5.63, 7.42, 7.53, 7.78 and 7.85%, respectively, in the dark system. As it can be seen from Fig. S8, NP-co-doped samples prepared from Soybean seeds show highest adsorption efficiency and ZC nanocomposite samples are the least, this result corroborates with the phenomena described elsewhere,[77] that as the surface area increases the sorption capacity of semiconductor photocatalyst raises; concurrently, adsorption capacity has also relation with surface charges, as N and P may be doped as N^{-3} and P^{-3} anion respectively on the surface of ZC nanostructure, hence the hydrolyzed positively charged crystal violet molecules may have higher tendency to adsorb on NP-co-doped ZC photocatalysts especially soybean-ZC as a result of its high N and P content[77].

The photocatalytic degradation efficiency of synthesized photocatalysts is in the order of: ZnO < ZC ≈ PhMx < sesame-ZC < rice-ZC < chickpea-ZC < soybean-ZC with corresponding values, 1.19, 39.24, 41.78, 76.69, 86.10, 91.74 and 96.38%, respectively using visible light in 120 min.

As shown in Fig. 5, the pure ZnO has no visible light photocatalytic activity, since its band gap energy is higher ≈ 3.30 eV (378 nm) which is far in the UV region, the visible photon cannot promote the VB electrons to CB as a result the photocatalytic activity of ZnO in the visible region is not accessible[53,78]. But the slight decrease in concentration of CV may be due to adsorption on ZnO surface during adsorption/desorption equilibrium before the sample is exposed to visible light for 30 min.

ZC nanocomposite photocatalyst shows red shift (2.85 eV) in the absorption wavelength range compared to ZnO (Fig. S5), which would improve its photocatalytic activity in the visible range. Thus, the ZC nanocomposite shows better degradation efficiency (Fig. 5). Since, the CB of CdO and ZnO are very close to each other, the injection of electrons from the CB of CdO into ZnO particles is expected to retard the back reaction between the photogenerated charge carriers[53]. This process of the hole trapping which is facilitated in the mixed semiconductor system would increase the efficiency. Thus, the efficiency of photogenerated electron-hole in ZC could be higher than that of ZnO. PhMx samples also show similar photocatalytic efficiency as ZC nanocomposite.

As it can be seen from Fig. 5, all the four NP-co-doped ZC nanocomposites show higher photocatalytic efficiency compared with ZnO and ZC nanocomposite samples due to highly extended band gap as a result of incorporation of N and P, which forms a localized state slightly above the valence band[79]. Additionally, surface P species may act as trapping sites to capture the e^-, leading to more effective separation of light-generated e^-/h^+ pairs and enhancement of photocatalytic activity[80,81]. The red shifts indicates photo-generated electrons and holes participating in the photocatalytic reactions could be excited by photons with lower energies, leading to high efficiency in photo-induced redox reaction of adsorbed substances[82]. Comparatively, the NP-co-doped ZC nanocomposites prepared from Soybean was the most visible photoactive, with a degradation efficiency of CV that reached 96.38% with standard deviation of ± 0.255 after 120 min of irradiation (Fig. S9 and Table S6) which may be due to highly extended band gap as a result of larger concentration doping of N and P. NP-co-doped ZC nanocomposite samples prepared from chickpea-ZC shows fairly similar photocatalytic degradation efficiency compared to soybean-ZC samples (Fig. 5), since leguminous seeds have higher contents of protein in turn N and P. Rice-ZC samples show second least photocatalytic activity as a result of lower concentration incorporation of N and P. In addition, sesame-ZC samples (Fig. 5) shows least photocatalytic efficiency which may be rationalized by lower concentration of N and P, and incorporation of impurities since sesame seeds are too small to remove the coat. Moreover, Table S7 presents a comparison of the selected photocatalyst with various composites based on ZnO and CdO for the degradation of photocatalytic pollutants. The photocatalytic test of optimization conditions such as pH of the solution (Fig. S10), CV dye concentration (Fig. S11), catalyst loading (Fig. S12), and the recyclability test (Fig. S13) are described in Supporting Information.

Kinetic study of photocatalysts

The kinetics of photodegradation of CV with various photocatalysts in visible light and dark conditions is demonstrated in Figs. 6 and S14, respectively. Kinetics of adsorption of CV with an initial concentration of 10 mg L^{-1} under no radiation and photocatalytic degradation under visible light irradiation follow pseudo-first-order kinetics. It is evident from the observed linear plots of $\ln{(C_o/C_t)}$ *versus* time given in (Figs. 6 and S14). The adsorption rate constants for CV using ZnO, ZC, PhMx, soybean-ZC, chickpea-ZC, sesame-ZC and rice-ZC without irradiation are: 6.37×10^{-4},9 3.90×10^{-4}, 3.99×10^{-4}, 6.38×10^{-4}, 6.01×10^{-4}, 6.78×10^{-4} and 4.75×10^{-4} min^{-1}, respectively. The rate constants for photocatalytic degradation of CV, under visible light irradiations, using ZnO, ZC, PhMx, soybean-ZC, chickpea-ZC, sesame-ZC and rice-ZC photocatalysts are: 1.02×10^{-4}, 4.0×10^{-3}, 4.0×10^{-3}, 2.76×10^{-2}, 1.98×10^{-2}, 1.22×10^{-2} and 1.57×10^{-2} min^{-1}, respectively. Fairly good correlation to the pseudo-first-order reaction kinetics ($R^2 \geq 0.951$) was found. Additionally, soybean-ZC samples have highest rate constant value suggesting that higher rate of photocatalytic degradation of CV by employing soybean-ZC samples. The rate laws expressions are described in Supporting Information.

Computational results

The band gap energy and the band structure of ZnO, $Zn_{0.9}Cd_{0.1}$ and NP co-doped $Zn_{0.9}Cd_{0.1}$ simulated samples were obtained by DFT method with generalized gradient approximation (GGA) for potential exchange correlation functional and double zeta polarized (DZP) basis set after geometry optimization with the same parameters except LDA for potential exchange correlation functional. The calculated band gap energy and band structure of the simulated samples are given in Table 1; Fig. 7, respectively.

The Cd, N and P ratios used in computational calculation are based on the results obtained from experimental data which are ZC (90:10 ratio) and 8–10% for N and P. Cd atoms were incorporated in ZnO lattice as

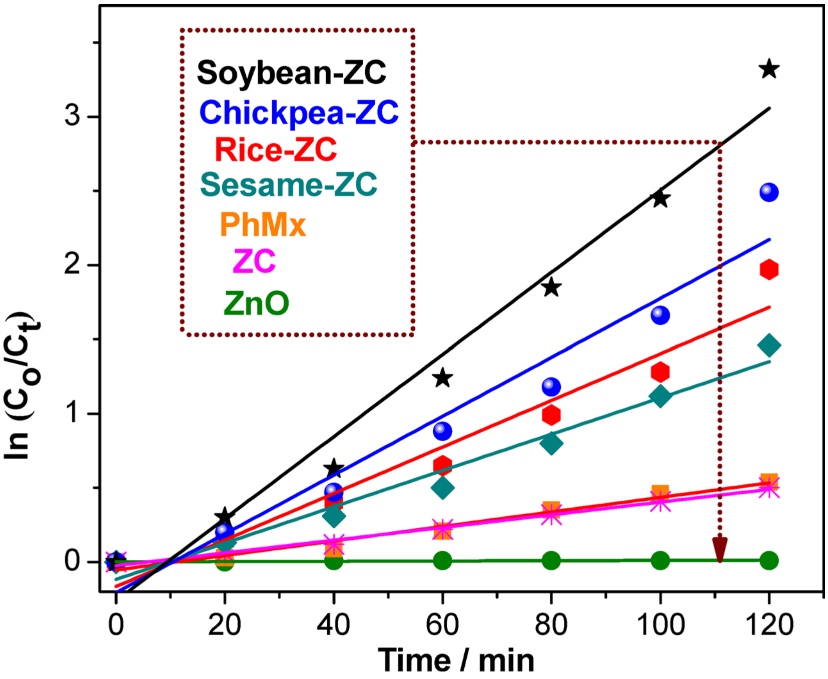

Fig. 6. Plot of $\ln(C_o/C_t)$ *versus* time for photodegradation of CV with visible light irradiation using different as-synthesized photocatalysts. Reaction conditions: initial CV concentration = 10 mg L^{-1}, catalyst load = 150 mg L^{-1}, pH = 7 and irradiation time = 120 min.

	This work				Other
Compound	**k-point**	**Γ_{VBM}**	**Γ_{CBM}**	**E_g (eV)**	**E_g (eV)**
ZnO	Γ_{21v}- Γ_{21c}	-0.4015	0.3699	0.77	0.82, 0.67
$Zn_{0.9}Cd_{0.1}O$	Γ_{21v}- Γ_{21c}	-0.0166	0.01757	0.03	-
$N_{0.08}P_{0.08}$- $Zn_{0.9}Cd_{0.1}O_{0.84}$	Γ_{21v}- Γ_{21c}	-0.0482	-0.0427	0.01	-
$N_{0.1}P_{0.08}$- $Zn_{0.9}Cd_{0.1}O_{0.82}$	Γ_{21v}- Γ_{21c}	-0.004	0.1181	0.12	-

Table 1. Band gap energy comparison of simulated samples.

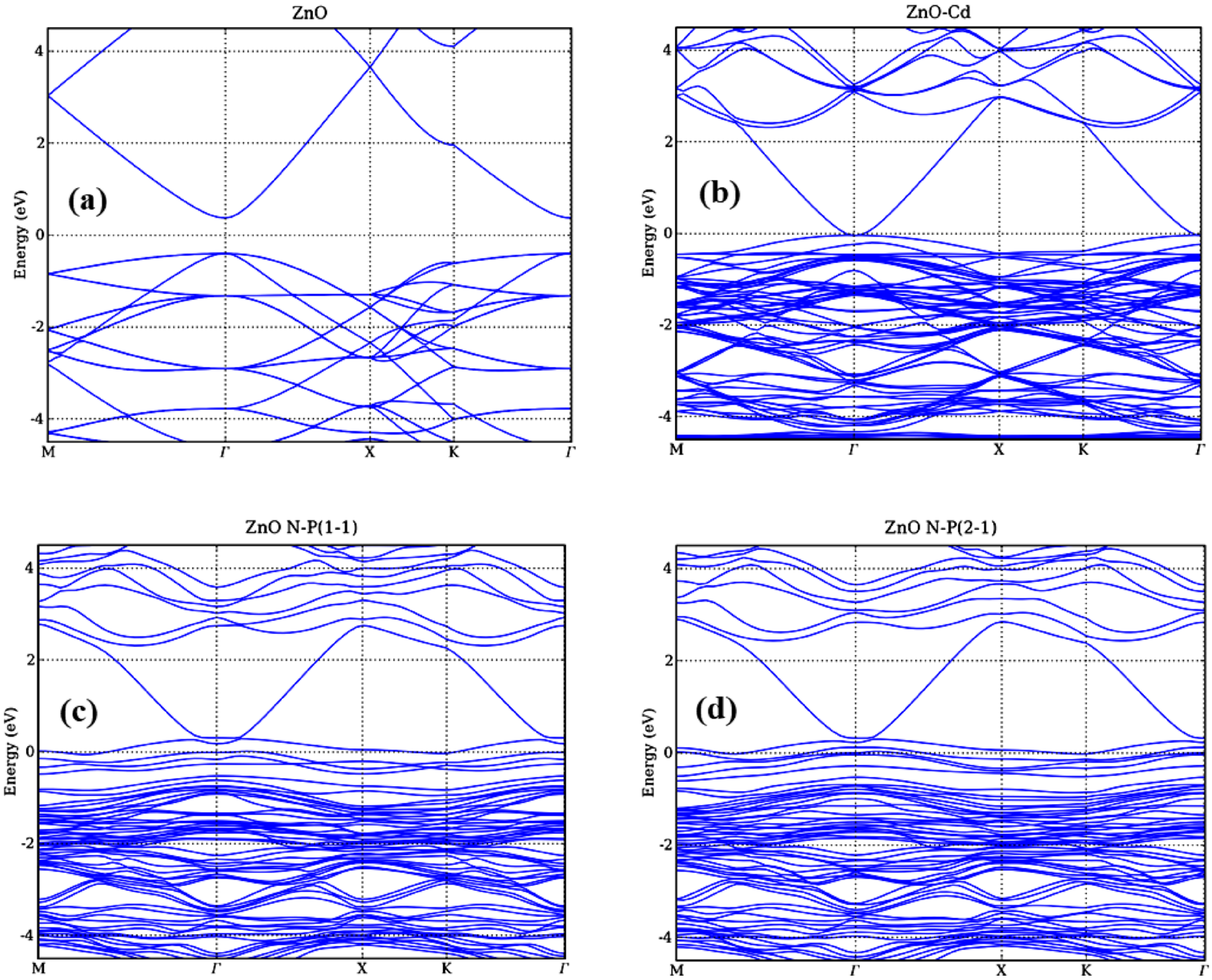

Fig. 7. DFT calculated band structures of simulated (**a**) ZnO, (**b**) $Zn_{0.9}Cd_{0.1}O$, (**c**) $N_{0.08}P_{0.08}$-$Zn_{0.9}Cd_{0.1}O_{0.84}$ and (**d**) $N_{0.1}P_{0.08}$-$Zn_{0.9}Cd_{0.1}O_{0.82}$ samples.

substitutional Cd in Zn-sites (Cd_{Zn}), whereas N and P were incorporated as substitutional N and P in O-sites (N_O and P_O) in $Zn_{0.9}Cd_{0.1}O$ lattice.

As it can be seen from Table 1, w-ZnO band structure with a direct Γ-point (k = 0) gap of 0.77 eV, here estimated as the difference between the Valence Band Maximum (VBM) (-0.4015 eV) and the Conduction Band Minimum (CBM) (0.3699 eV) indicating that ZnO is a direct band gap semiconductor (Fig. 7a). These results are in very good agreement with most theoretical predictions based on conventional DFT calculations[83–85], where the size of the w-ZnO band gap is strongly underestimated with respect to experimental results, possible reason for this discrepancy might be the fact that the band gap problem of LDA/GGA functional[84].

The band gap of $Zn_{0.9}Cd_{0.1}O$ is 0.03 eV, which showed large red-shift compared to pure ZnO. This is the result of Cd incorporation into ZnO lattice in which Cd atom has larger number of electrons in addition to its larger size. As can be seen from Fig. 7b, the conduction band minima is deep down to the Fermi level which supports the experimental result even if it is strongly underestimated.

Fig. 7c-d shows the band structures of $N_{0.08}P_{0.08}$-$Zn_{0.9}Cd_{0.1}O_{0.84}$ and $N_{0.1}P_{0.08}$-$Zn_{0.9}Cd_{0.1}O_{0.82}$, respectively. As can be seen in both cases the conduction band minima (CBM) and valence band maxima (VBM) of both samples are very close to the Fermi level as a result the transition of an electron from valence band to conduction band will need less energy; 0.01 eV and 0.12 eV, respectively, which may be the result of N and P incorporation that creates shallow donors and acceptors near the Fermi level. The reduced band gap of ZnO due to coupling with CdO and N and P co-doping is verified by experimental results upon characterization and application of the synthesized samples on photocatalytic degradation of crystal violet dye; the computational results also confirmed the feasibility of CdO coupling and, N and P co-doping for ZnO band gap reduction.

Conclusions

In the present study, nanosized ZnO, CdO, ZC and biogenic NP-co-doped ZC nanocomposites were synthesized using thermal decomposition method. The biogenic NP-co-doped ZC nanocomposites were synthesized by employing leguminous crop seeds such as Sesame, Chickpea, Soybean and Rice. The use of biogenic synthesis, employing plant extracts as reducing and stabilizing agents, makes the process sustainable and economically viable, as it eliminates the need for expensive and toxic chemicals. The as-synthesized photocatalysts were characterized by PXRD, XPS, TGA, SEM, Cs-corrected STEM-HAADF, EDS, AAS, FTIR and UV-vis absorption spectra. Doping of N and P into ZC nanocomposites results in change in the electronic properties of ZC leading to well extended optical absorption to the visible wavelength region which ameliorate harvesting of more photons of visible wavelength; concurrently, improving the photocatalytic activity of the semiconductor. DFT calculation results also confirmed that the incorporation of N and P have positively influenced the absorption band gap of ZC nanostructures. Biogenic N and P doping into ZC showed a positive influence on the photocatalytic degradation of crystal violet by facilitating electron-hole pair separation due to their trapping ability of photogenerated electron. As-synthesized NP-co-doped ZC showed higher photoactivity than the ZC nanocomposite as well as calcined ZnO in visible irradiation; this may be due to the synergetic cumulative effect of N and P co-doping in ZC that enhances the photocatalytic degradation of crystal violet with good recyclability further enhance their economic feasibility. Thus, it can be used for the synthesis of other nanocomposite photocatalysts. The photocatalytic degradation of crystal violet using as-synthesized nanomaterials follows pseudo-first order kinetics. In addition, this study offers significant societal benefits by providing an efficient, eco-friendly, and cost-effective solution for environmental remediation, particularly in the degradation of organic pollutants like crystal violet.

Data availability

Our data included electronically as supplementary materials and if necessary the other research data will be made available on reasonable request from the corresponding author, Jemal M. Yassin.

Received: 4 January 2025; Accepted: 6 May 2025

References

1. Baig, N., Kammakakam, I., Falath, W. & Nanomaterials A review of synthesis methods, properties, recent progress, and challenges. *Mater. Adv.* **2**, 1821–1871. https://doi.org/10.1039/D0MA00807A (2021).
2. Pokrajac, L. et al. Nanotechnology for a sustainable future: addressing global challenges with the international network4sustainable nanotechnology. *ACS Nano.* **5**, (2021).
3. Gohar, O. et al. Nanomaterials for advanced energy applications: recent advancements and future trends. *Mater. Des.* **241**, 112930. https://doi.org/10.1016/j.matdes.2024.112930 (2024).
4. Naseem, T. & Durrani, T. The role of some important metal oxide nanoparticles for wastewater and antibacterial applications: A review. *Environ. Chem. Ecotoxicol.* **3**, 59–75. https://doi.org/10.1016/j.enceco.2020.12.001 (2021).
5. Gao, C. et al. Heterogeneous single-atom photocatalysts: fundamentals and applications. *Chem. Rev.* **120**, 12175–12216. https://doi.org/10.1021/acs.chemrev.9b00840 (2020).
6. 6 Herrmann, J. M. Heterogeneous photocatalysis: fundamentals and applications to the removal of various types of aqueous pollutants. *Catal. Today*. **53**, 115–129. https://doi.org/10.1016/S0920-5861(99)00107-8 (1999).
7. Wang, Z., Li, C. & Domen, K. Recent developments in heterogeneous photocatalysts for solar-driven overall water splitting. *Chem. Soc. Rev.* **48**, 2109–2125. https://doi.org/10.1039/C8CS00542G (2019).
8. Alam, M. W. et al. Novel Nd-N/TiO_2 nanoparticles for photocatalytic and antioxidant applications using hydrothermal approach. *Materials* **15**, 6658. https://doi.org/10.3390/ma15196658 (2022).
9. Gu, C., Jia, A. B., Zhang, Y. M. & Zhang, S. X.-A. Emerging electrochromic materials and devices for future displays. *Chem. Rev.* **122**, 14679–14721. https://doi.org/10.1021/acs.chemrev.1c01055 (2022).
10. Yoon, J. et al. Heterogeneously integrated optoelectronic devices enabled by micro-transfer printing. *Adv. Opt. Mater.* **3**, 1313–1335. https://doi.org/10.1002/adom.201500365 (2015).
11. BaQais, A. et al. Probe-sonicated synthesis of CuO–ZnO hybrid nanocomposite for photocatalytic and supercapacitor applications. *Inorganics* **11**, 370. https://doi.org/10.3390/inorganics11090370 (2023).
12. Shalygina, E. et al. Magnetic-field behavior of heterogeneous magnetic materials. *J. Magn. Magn. Mater.* **321**, 865–867. https://doi.org/10.1016/j.jmmm.2008.11.052 (2009).
13. 13 Zhang, Q., Yang, X. & Guan, J. Applications of magnetic nanomaterials in heterogeneous catalysis. *ACS Appl. Nano Mater.* **2**, 4681–4697. https://doi.org/10.1021/acsanm.9b00976 (2019).
14. Samal, K., Mahapatra, S. & Ali, M. H. Pharmaceutical wastewater as emerging contaminants (EC): treatment technologies, impact on environment and human health. *Energy Nexus*. **100076** https://doi.org/10.1016/j.nexus.2022.100076 (2022).
15. Zelekew, O. A., Kuo, D. H., Yassin, J. M., Ahmed, K. E. & Abdullah, H. Synthesis of efficient silica supported TiO_2/Ag_2O heterostructured catalyst with enhanced photocatalytic performance. *Appl. Surf. Sci.* **410**, 454–463. https://doi.org/10.1016/j.apsusc.2017.03.089 (2017).
16. Aldughaylibi, F. S. et al. Extraction of bioactive compounds for antioxidant, antimicrobial, and antidiabetic applications. *Molecules* **27**, 5935. https://doi.org/10.3390/molecules27185935 (2022).
17. Richardson, S. D. & Kimura, S. Y. Water analysis: emerging contaminants and current issues. *Anal. Chem.* **92**, 473–505. https://doi.org/10.1021/acs.analchem.5b04493 (2019).

18. Kumar, V. et al. Environmental impact, health hazards, and plant-microbes synergism in remediation of emerging contaminants. *Clean. Chem. Eng.* **100030** https://doi.org/10.1016/j.clce.2022.100030 (2022).
19. Konstantinou, I. K. & Albanis, T. A. TiO_2-assisted photocatalytic degradation of Azo dyes in aqueous solution: kinetic and mechanistic investigations: a review. *Appl. Catal. B: Environ.* **49**, 1–14. https://doi.org/10.1016/j.apcatb.2003.11.010 (2004).
20. Lord, M. D., Neve, G., Keating, M. & Budhathoki-Uprety, J. Polycarbodiimide for textile dye removal from contaminated water. *ACS Appl. Polym. Mater.* **4**, 6192–6201. https://doi.org/10.1021/acsapm.2c00959 (2022).
21. Ansari, M. O., Khan, M. M., Ansari, S. A. & Cho, M. H. Electrically conductive polyaniline sensitized defective-TiO_2 for improved visible light photocatalytic and photoelectrochemical performance: a synergistic effect. *New. J. Chem.* **39**, 8381–8388. https://doi.org/10.1039/C5NJ01127B (2015).
22. Castillo-Suárez, L., Sierra-Sánchez, A., Linares-Hernández, I., Martínez-Miranda, V. & Teutli-Sequeira, E. A critical review of textile industry wastewater: green technologies for the removal of Indigo dyes. *Int. J. Environ. Sci. Technol.* 1–38. https://doi.org/10.1007/s13762-023-04810-2 (2023).
23. Munawar, T. et al. Sunlight-activated Mo-doped La_2CuO_4/rGO perovskite oxide nanocomposite for photocatalytic treatment of diverse dyes pollutant. *Mater. Sci. Eng. B.* **304**, 117355. https://doi.org/10.1016/j.mseb.2024.117355 (2024).
24. Bayrakdar, M., Atalay, S. & Ersöz, G. Efficient treatment for textile wastewater through sequential photo Fenton-like oxidation and adsorption processes for reuse in irrigation. *Ceram. Int.* **47**, 9679–9690. https://doi.org/10.1016/j.ceramint.2020.12.107 (2021).
25. Coha, M., Farinelli, G., Tiraferri, A., Minella, M. & Vione, D. Advanced oxidation processes in the removal of organic substances from produced water: potential, configurations, and research needs. *Chem. Eng. J.* **414**, 128668. https://doi.org/10.1016/j.cej.2021.128668 (2021).
26. Byrne, C., Subramanian, G. & Pillai, S. C. Recent advances in photocatalysis for environmental applications. *J. Environ. Chem. Eng.* **6**, 3531–3555. https://doi.org/10.1016/j.jece.2017.07.080 (2018).
27. Lou, S. N., Lim, J., Jeon, T. H. & Choi, W. Designing Eco-functional redox conversions integrated in environmental photo (electro) catalysis. *ACS EST. Engg.* **2**, 1116–1129. https://doi.org/10.1021/acsestengg.2c00009 (2022).
28. Nunes, D., Pimentel, A., Branquinho, R., Fortunato, E. & Martins, R. Metal oxide-based photocatalytic paper: A green alternative for environmental remediation. *Catalysts* **11**, 504. https://doi.org/10.3390/catal11040504 (2021).
29. Ansari, S. A. et al. Emerging NiO–rGO nanohybrids for antibiotic pollutant degradation under visible-light irradiation. *Surf. Interfaces*. **40**, 103078. https://doi.org/10.1016/j.surfin.2023.103078 (2023).
30. Hintsho, N., Petrik, L., Nechaev, A., Titinchi, S. & Ndungu, P. Photo-catalytic activity of titanium dioxide carbon nanotube nano-composites modified with silver and palladium nanoparticles. *Appl. Catal. B: Environ.* **156**, 273–283. https://doi.org/10.1016/j.apcatb.2014.03.021 (2014).
31. Yousef, A. et al. Encapsulation of CdO/ZnO NPs in PU electrospun nanofibers as novel strategy for effective immobilization of the photocatalysts. *Colloids Surf. A: Physicochem Eng. Asp.* **401**, 8–16. https://doi.org/10.1016/j.colsurfa.2012.02.033 (2012).
32. 32 Hatamie, A. et al. Zinc oxide nanostructure-modified textile and its application to biosensing, photocatalysis, and as antibacterial material. *Langmuir* **31**, 10913–10921. https://doi.org/10.1021/acs.langmuir.5b02341 (2015).
33. Kebede, T., Taddesse, A. M., Geresu, G., Diaz, I. & Yassin, J. M. Boosted photocatalytic and antibacterial activities of polyaniline supported tandem Nn ternary CdS-ZnO-Ag_3PO_4 composite under visible light irradiation. *J. Environ. Chem. Eng.* **110338** https://doi.org/10.1016/j.jece.2023.110338 (2023).
34. Munawar, T. et al. Boosted charge separation via Ce_2S_3 over dual Z-scheme ZnO–Ce_2S_3–MnO_2 core double-shell nanocomposite for the degradation of diverse dye pollutants. *Environ. Res.* **251**, 118675. https://doi.org/10.1016/j.envres.2024.118675 (2024).
35. Hagfeldt, A. & Graetzel, M. Light-induced redox reactions in nanocrystalline systems. *Chem. Rev.* **95**, 49–68. https://doi.org/10.1021/cr00033a003 (1995).
36. Saravanan, R. et al. ZnO/Ag/CdO nanocomposite for visible light-induced photocatalytic degradation of industrial textile effluents. *J. Colloid Interface Sci.* **452**, 126–133. https://doi.org/10.1016/j.jcis.2015.04.035 (2015).
37. Kavasoglu, N., Kavasoglu, A. S. & Oktik, S. Observation of negative photoconductivity in $(ZnO)_x(CdO)_{1-X}$ films. *J. Phys. Chem. Solids*. **70**, 521–526. https://doi.org/10.1016/j.jpcs.2008.11.018 (2009).
38. Smith, A. M. & Nie, S. Semiconductor nanocrystals: structure, properties, and band gap engineering. *Acc. Chem. Res.* **43**, 190–200. https://doi.org/10.1021/ar9001069 (2010).
39. Serpone, N. & Emeline, A. **3** 673–677 (*J. Phys. Chem. Lett.*, (2012).
40. Li, B. & Wang, Y. Facile synthesis and photocatalytic activity of ZnO–CuO nanocomposite. *Superlattices Microstruct.* **47**, 615–623. https://doi.org/10.1016/j.spmi.2010.02.005 (2010).
41. Chakravorty, A. & Roy, S. A. Review of-Photocatalysis, basic principles, processes, and materials. *Sustain. Chem. Environ.* **100155** https://doi.org/10.1016/j.scenv.2024.100155 (2024).
42. Kumar, A., Choudhary, P., Kumar, A., Camargo, P. H. & Krishnan, V. Recent advances in plasmonic photocatalysis based on TiO_2 and noble metal nanoparticles for energy conversion, environmental remediation, and organic synthesis. *Small* **18**, 2101638. https://doi.org/10.1002/smll.202101638 (2022).
43. Jiang, Z. et al. Recent advances and perspectives of emerging two-dimensional transition metal carbide/nitride-based materials for organic pollutant photocatalysis. *Mater. Chem. Front.* https://doi.org/10.1039/D3QM00288H (2023).
44. Nadeem, M. S. et al. Effect of Co/Nd co-doping on the structural, optical, and morphological properties of ZnO nanorods grown on silicon substrate Si (100) by hydrothermal method. *J. Lumin.* **269**, 120484. https://doi.org/10.1016/j.jlumin.2024.120484 (2024).
45. Negash, A., Derseh, L. M., Tedla, A. & Yassin, J. M. Eco-friendly synthesis of CuO/Bi_2O_3 nanocomposite for efficient photocatalytic degradation of Rhodamine B dye. *Sci. Rep.* **14**, 23393. https://doi.org/10.1038/s41598-024-74408-2 (2024).
46. Rehman, S., Ullah, R., Butt, A. & Gohar, N. Strategies of making TiO_2 and ZnO visible light active. *J. Hazard. Mater.* **170**, 560–569. https://doi.org/10.1016/j.jhazmat.2009.05.064 (2009).
47. Banerjee, S. et al. New insights into the mechanism of visible light photocatalysis. *J. Phys. Chem. Lett.* **5**, 2543–2554. https://doi.org/10.1021/jz501030x (2014).
48. 48 Klingshirn, C. F., Waag, A., Hoffmann, A. & Geurts, J. Zinc oxide: from fundamental properties towards novel applications. (2010). https://doi.org/10.1007/978-3-642-10577-7
49. Raha, S. & Ahmaruzzaman, M. ZnO nanostructured materials and their potential applications: progress, challenges and perspectives. *Nanoscale Adv.* **4**, 1868–1925. https://doi.org/10.1039/D1NA00880C (2022).
50. Yashwanth, H. et al. Synergy between nitrogen, phosphorus co-doped carbon quantum Dots and ZnO nanorods for enhanced hydrogen production. *J. Alloys Compd.* **937**, 168397. https://doi.org/10.1016/j.jallcom.2022.168397 (2023).
51. Kati, N. Controlling of optical band gap of the CdO films by zinc oxide. *Mater. Sci.* **37**, 136–141. https://doi.org/10.2478/msp-2018-0104 (2019).
52. Acosta, D., López-Suárez, A., Magaña, C. & Hernández, F. Structural, electrical and optical properties of ZnO thin films produced by chemical spray using ethanol in different amounts of the sprayed solution. *Thin Solid Films*. **653**, 309–316. https://doi.org/10.1016/j.tsf.2018.03.031 (2018).
53. Saravanan, R., Shankar, H., Prakash, T., Narayanan, V. & Stephen, A. ZnO/CdO composite nanorods for photocatalytic degradation of methylene blue under visible light. *Mater. Chem. Phys.* **125**, 277–280. https://doi.org/10.1016/j.matchemphys.2010.09.030 (2011).
54. Kader, S., Al-Mamun, M. R., Suhan, M. B. K., Shuchi, S. B. & Islam, M. S. Enhanced photodegradation of Methyl orange dye under UV irradiation using MoO_3 and ag doped TiO_2 photocatalysts. *Environ. Technol. Inno.* **27**, 102476. https://doi.org/10.1016/j.eti.2022.102476 (2022).

55. Zhao, T., Chen, J., Wang, X. & Yao, M. Enhanced photocatalytic activity of MoS_2 via N + F codoping and strain engineering: A first-principles investigation. *Appl. Surf. Sci.* **607**, 154881. https://doi.org/10.1016/j.apsusc.2022.154881 (2023).
56. Kumari, R., Sahai, A. & Goswami, N. Effect of nitrogen doping on structural and optical properties of ZnO nanoparticles. *Prog Nat. Sci. : Mater. Int.* **25**, 300–309. https://doi.org/10.1016/j.pnsc.2015.08.003 (2015).
57. Abebe, B. & Murthy, H. A. Insights into ZnO-based doped porous nanocrystal frameworks. *RSC Adv.* **12**, 5816–5833. https://doi.org/10.1039/D1RA09152B (2022).
58. Panigrahy, B. & Bahadur, D. -type phosphorus doped ZnO nanostructures: an electrical, optical, and magnetic properties study. *RSC Adv.* **2**, 6222–6227. https://doi.org/10.1039/C2RA20441J (2012).
59. Sangwongchai, W., Tananuwong, K., Krusong, K., Natee, S. & Thitisaksakul, M. Starch chemical composition and molecular structure in relation to physicochemical characteristics and resistant starch content of four Thai commercial rice cultivars differing in pasting properties. *Polymers* **15**, 574. https://doi.org/10.3390/polym15030574 (2023).
60. Gurbani, N. & Chouhan, N. P–N heterojunction system Eu-Doped ZnO@GO for photocatalytic water splitting. *Global Chall.* **7**, 2200106. https://doi.org/10.1002/gch2.202200106 (2023).
61. Chavillon, B. et al. P-type nitrogen-doped ZnO nanoparticles stable under ambient conditions. *J. Am. Chem. Soc.* **134**, 464–470. https://doi.org/10.1021/ja208044k (2012).
62. Singh, S., Sharma, R. & Mehta, B. R. Enhanced surface area, high Zn interstitial defects and band gap reduction in N-doped ZnO nanosheets coupled with $BiVO_4$ leads to improved photocatalytic performance. *Appl. Surf. Sci.* **411**, 321–330. https://doi.org/10.1016/j.apsusc.2017.03.189 (2017).
63. Han, T., Fan, T., Chow, S. K. & Zhang, D. Biogenic N–P-codoped TiO_2: synthesis, characterization and photocatalytic properties. *Bioresour Technol.* **101**, 6829–6835. https://doi.org/10.1016/j.biortech.2010.03.107 (2010).
64. Hu, D. et al. Synthesis of location-dependent phosphorus-doped ZnO nanostructures on the porous alumina membranes. *Phys. Status Solidi (a).* **211**, 856–861. https://doi.org/10.1002/pssa.201330159 (2014).
65. Kim, C. S. et al. Synthesis and characterization of Cu/N-doped mesoporous TiO_2 visible light photocatalysts. *Appl. Catal. Gen.* **455**, 211–218. https://doi.org/10.1016/j.apcata.2013.01.041 (2013).
66. Pratheepa, M. I. & Lawrence, M. Synthesis of pure, Cu and Zn doped CdO nanoparticles by co-precipitation method for supercapacitor applications. *Vacuum* **162**, 208–213. https://doi.org/10.1016/j.vacuum.2019.01.042 (2019).
67. Mandor, H., Amin, N. K., Abdelwahab, O. & El-Ashtoukhy, E. S. Z. Preparation and characterization of N-doped ZnO and N-doped TiO_2 beads for photocatalytic degradation of phenol and ammonia. *Environ. Sci. Pollut Res.* **29**, 56845–56862. https://doi.org/10.1007/s11356-022-19421-6 (2022).
68. Saussey, J., Lavalley, J. C. & Bovet, C. Infrared study of CO_2 adsorption on ZnO. Adsorption sites. *J. Chem. Soc. Faraday Trans.* **1 78**, 1457–1463. https://doi.org/10.1039/F19827801457 (1982).
69. John, R., Shanmugaraj, S. F., Rajaram, R. & Endo, T. Synthesis and characterization of nano ZnO and CdO. *J. Ceram. Soc. Jpn*. **118**, 329–332. https://doi.org/10.2109/jcersj2.118.329 (2010).
70. Yuan, G. et al. p-Type conduction in Al–N co-doped ZnO films. *Mater. Lett.* **58**, 3741–3744. https://doi.org/10.1016/j.matlet.2004.02.056 (2004).
71. Shao, G. S., Wang, F. Y., Ren, T. Z., Liu, Y. & Yuan, Z. Y. Hierarchical mesoporous phosphorus and nitrogen doped Titania materials: synthesis, characterization and visible-light photocatalytic activity. *Appl. Catal. B: Environ.* **92**, 61–67. https://doi.org/10.1016/j.apcatb.2009.07.024 (2009).
72. Kim, H. et al. Pulsed laser deposition of Zr–N codoped p-type ZnO thin films. *Appl. Phys. A.* **93**, 593–598. https://doi.org/10.1007/s00339-008-4711-z (2008).
73. Shifu, C., Wei, Z., Sujuan, Z. & Wei, L. Preparation, characterization and photocatalytic activity of N-containing ZnO powder. *J. Chem. Eng.* **148**, 263–269. https://doi.org/10.1016/j.cej.2008.08.039 (2009).
74. Swapna, R. & Kumar, M. S. Deposition of Na–N dual acceptor doped p-type ZnO thin films and fabrication of p-ZnO:(Na, N)/n-ZnO: Eu homojunction. *Mater. Sci. Eng. B.* **178**, 1032–1039. https://doi.org/10.1016/j.mseb.2013.06.010 (2013).
75. Ravichandran, K., Mohan, R., Begum, N. J., Swaminathan, K. & Ravidhas, C. Property enhancement of transparent conducting zinc oxide thin films—Effect of simultaneous (Sn + F) doping. *J. Phys. Chem. Solids.* **74**, 1794–1801. https://doi.org/10.1016/j.jpcs.2013.07.010 (2013).
76. Ahmad, M. et al. A facile one-step approach to synthesizing ZnO/graphene composites for enhanced degradation of methylene blue under visible light. *Appl. Surf. Sci.* **274**, 273–281. https://doi.org/10.1016/j.apsusc.2013.03.035 (2013).
77. Tajizadegan, H., Jafari, M., Rashidzadeh, M. & Saffar-Teluri, A. A high activity adsorbent of ZnO–Al_2O_3 nanocomposite particles: synthesis, characterization and dye removal efficiency. *Appl. Surf. Sci.* **276**, 317–322. https://doi.org/10.1016/j.apsusc.2013.03.089 (2013).
78. Liu, W., Wang, M., Xu, C., Chen, S. & Fu, X. Ag_3PO_4/ZnO: an efficient visible-light-sensitized composite with its application in photocatalytic degradation of Rhodamine B. *Mater. Res. Bull.* **48**, 106–113. https://doi.org/10.1016/j.materresbull.2012.10.015 (2013).
79. Di Valentin, C., Pacchioni, G., Selloni, A., Livraghi, S. & Giamello, E. Characterization of paramagnetic species in N-doped TiO_2 powders by EPR spectroscopy and DFT calculations. *J. Phys. Chem. B.* **109**, 11414–11419. https://doi.org/10.1021/jp051756t (2005).
80. Wang, W. et al. In situ protonated-phosphorus interstitial doping induces long-lived shallow charge trapping in porous $C_{3-x}N_4$ photocatalysts for highly efficient H_2 generation. *Energy Environ. Sci.* **16**, 460–472. https://doi.org/10.1039/d2ee02680e (2023).
81. Zheng, R. et al. Novel thermally stable phosphorus-doped TiO_2 photocatalyst synthesized by hydrolysis of $TiCl_4$. *J. Mol. Catal. Chem.* **319**, 46–51. https://doi.org/10.1016/j.molcata.2009.11.019 (2010).
82. Hashimoto, K., Irie, H. & Fujishima, A. TiO_2 photocatalysis: a historical overview and future prospects. *Jpn J. Appl. Phys.* **44**, 8269. https://doi.org/10.1143/JJAP.44.8269 (2005).
83. Jafarova, V. & Orudzhev, G. Structural and electronic properties of ZnO: A first-principles density-functional theory study within LDA (GGA) and LDA (GGA) + U methods. *Solid State Commun.* **325**, 114166. https://doi.org/10.1016/j.ssc.2020.114166 (2021).
84. Moreira, N. H. Computational studies on functionalized ZnO surfaces and nanostructures, *Bremen, Univ., Diss.* (2011).
85. Clark, S. J. & Robertson, J. Screened exchange density functional applied to solids. *Phys. Rev. B Condens. Matter.* **82**, 085208. https://doi.org/10.1103/PhysRevB.82.085208 (2010).

Acknowledgements

The authors acknowledge the grant PID2022-136321OB-C21/AEI/10.13039/501100011033/FEDER, EU and to the PID2022-136535OB-100 grant; to the CSIC for the COOPA20271, COOPB22002, and COOPB24072 grants, as well as research grants (HURG-2016-03-02 and HURG-2020-03-02-75) received from Ministry of Education through office of the Research and Extension, Haramaya University. AM acknowledges the Spanish Ministry of Science (RYC2018-024561-I and to the European Union NextGeneration EU/PTR; CNS2023-144346), the grant CEX2023-001286-S funded by MICIU/AEI/10.13039/501100011033 and the support by Aragon Government (E13_23R). Authors acknowledge the use of instrumentation as well as the technical advice provided by the National Facility ELECMI ICTS node "Laboratorio de Microscopías Avanzadas" at the University of Zaragoza.

Author contributions

G.N.: Methodology, Investigation, Writing first draft; A.M.T. Conceptualization, Methodology, Data-curation, Writing-Reviewing, Editing; I.D. Conceptualization, Data-curation, Writing-Reviewing, Editing; A.M.M. Conceptualization, Methodology, Data-curation, Software, Formal analysis, Writing-Reviewing, Editing; Á.M. Conceptualization, Methodology, Data-curation, Software, Formal analysis, Writing-Reviewing, Editing; and J.M.Y.: Conceptualization, Methodology, Data-curation, Software, Formal analysis, Writing-Reviewing, Editing.

Declarations

Competing interests

The authors declare no competing interests.

Additional information

Supplementary Information The online version contains supplementary material available at https://doi.org/10.1038/s41598-025-01403-6.

Correspondence and requests for materials should be addressed to A.M.T. or J.M.Y.

Reprints and permissions information is available at www.nature.com/reprints.

Publisher's note Springer Nature remains neutral with regard to jurisdictional claims in published maps and institutional affiliations.

Open Access This article is licensed under a Creative Commons Attribution-NonCommercial-NoDerivatives 4.0 International License, which permits any non-commercial use, sharing, distribution and reproduction in any medium or format, as long as you give appropriate credit to the original author(s) and the source, provide a link to the Creative Commons licence, and indicate if you modified the licensed material. You do not have permission under this licence to share adapted material derived from this article or parts of it. The images or other third party material in this article are included in the article's Creative Commons licence, unless indicated otherwise in a credit line to the material. If material is not included in the article's Creative Commons licence and your intended use is not permitted by statutory regulation or exceeds the permitted use, you will need to obtain permission directly from the copyright holder. To view a copy of this licence, visit http://creativecommons.org/licenses/by-nc-nd/4.0/.

© The Author(s) 2025